

Unveiling the chirality of the quantum anomalous Hall effect

Hongyu Chen,¹ Yuanjun Jin¹,,¹ Mohammad Yahyavi,¹ Ilya Belopolski,² Sen Shao,¹ Tao Hou,¹ Naizhou Wang,¹ Chia-Hsiu Hsu,¹ Yilin Zhao,¹ Bo Yang,¹ Qiong Ma,³ Jia-Xin Yin,⁴ Su-Yang Xu,⁵ Wei-bo Gao,¹ and Guoqing Chang^{1,*}

¹*Division of Physics and Applied Physics, School of Physical and Mathematical Sciences, Nanyang Technological University, Singapore 637371, Singapore*

²*RIKEN Center for Emergent Matter Science (CEMS), Wako, Saitama 351-0198, Japan*

³*Department of Physics, Boston College, Chestnut Hill, Massachusetts 02467, USA*

⁴*Department of Physics, Southern University of Science and Technology, Shenzhen, Guangdong 518055, China*

⁵*Department of Chemistry and Chemical Biology, Harvard University, Cambridge, Massachusetts, USA*



(Received 28 December 2023; accepted 22 February 2024; published 12 March 2024)

The ordinary and quantum Hall effects with fixed carrier types, electron or hole, exhibit well-defined chirality under external magnetic fields, but the analogous chirality of the quantum anomalous Hall effect (QAHE) remains little explored. Here, for the electronic structures of intrinsic QAHE systems, we show that the local Berry curvature is linked with the angular-momentum difference $l_{\delta z}$ of the inverted bands. In the presence of rotation symmetries, the value of $l_{\delta z}$ will be quantized and set as the Chern number. The quantized $l_{\delta z}$ will also give rise to a unique quantized magnetic circular dichroism effect in the case of resonance absorption. By $l_{\delta z}$, we find that the chiral flow-direction of an electron in the QAHE is not explicitly related to the intrinsic spin axis, thereby enabling the spin-momentum-unlocking edge states in an antiferromagnetic QAHE system. The validity of our theory is confirmed through rigorous examinations using perturbation theory, $\mathbf{k} \cdot \mathbf{p}$ modeling, tight-binding modeling, and first-principle calculations, which predicts exotic behavior in experimentally accessible quantum materials.

DOI: [10.1103/PhysRevB.109.125305](https://doi.org/10.1103/PhysRevB.109.125305)

The investigation of quantized Hall conductance, which is one of the key fields of condensed matter physics, opens the door to study topological quantum materials [1–24]. The quantum Hall effect (QHE) is a consequence of Landau orbits and related chiral edge modes under strong external magnetic fields [1–3]. Researchers found that the quantized Hall conductance can also be realized without external magnetic fields, namely, the quantum anomalous Hall effect (QAHE) [4–6]. The QAHE was experimentally realized by doping magnetic Cr impurities into thin films of Bi₂Te₃-based topological insulators (TIs) [6]. Since then, intensive attention has been paid to searching for candidates for quantum anomalous Hall insulators (QAHIs) with internal magnetic moments [7–10,25].

In the QHE, the flow of the Hall current is directly determined by the flux of external magnetic fields. In contrast, the connection between the anomalous Hall current and internal magnetization remains elusive [6,24,26]. For instance, despite very similar crystal and electronic structures, the anomalous Hall conductivity in Cr- and Mn-doped Sb₂Te₃ are of opposite signs under the same magnetization direction and carrier types [6,24,26]. Furthermore, when approaching net zero magnetic moments, the QAHE has also been observed in noncollinear antiferromagnetic (AFM) Mn₃Sn [27], suggesting the possibility of realizing a QAH with net zero magnetization [28,29]. Additionally, magnetization easy-axis

and temperature can both induce the sign change of the Chern number [30,31], but the microscopic mechanism is still unclear. All these observations show that internal magnetization is associated with the anomalous Hall conductivity indirectly. Therefore, it is interesting to ask if there is another hidden internal variable which dominates the flow direction of the Hall current in QAHE.

Here, in the intrinsic electronic structures of QAHIs, we find that a unique angular-momentum difference $l_{\delta z}$ between the electron and hole of the inverted bands is linked with the local Berry curvature. Analytically, in the presence of rotation symmetries, we show that this critical $l_{\delta z}$ is directly proportional to the Chern number such as $|l_{\delta z}| = 2$, giving rise to quadratic dispersion and a diploid Chern number in linear dispersion from $|l_{\delta z}| = 1$. This Hall conductance $l_{\delta z}$ correspondence makes the magnetic circular dichroism effect a detection technology for QAHIs. All these conclusions are successfully verified by the lattice tight-binding model and first-principles calculations of real materials. Based on our discovered decoupling between the flow direction of the Hall current and the intrinsic spin axis of an electron, an AFM QAH is made by two ferromagnetic ones with opposite $l_{\delta z}$'s, and the two edge states break the locking between the spin and the momentum.

In the electronic structure of an intrinsic QAH, spin-polarized bands cross at the band crossing point, mix and gap because of spin-orbit coupling (SOC), and give rise to large local Berry curvature at the band crossing point. To figure out how ubiquitous variables such as spin and orbital angular

*Corresponding author: guoqing.chang@ntu.edu.sg

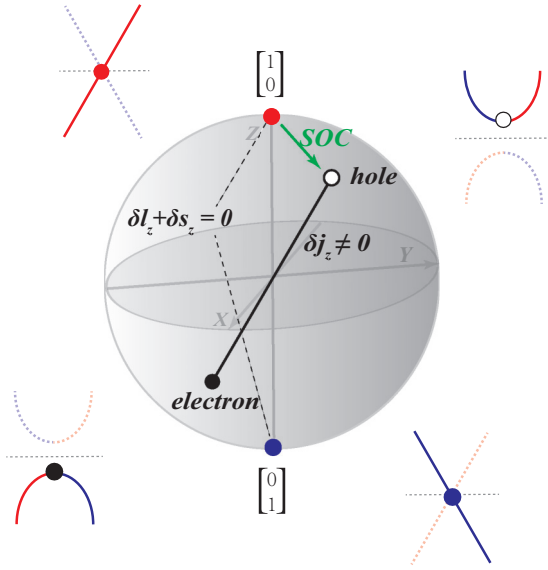


FIG. 1. The simultaneous Berry phase and δj_z from bands crossing and interlevel spin-orbit coupling (SOC) interaction. Two pure states (solid red and blue dots at north and south poles) and two mixing states (solid black and hollow dots which are far away from the poles) are on a Bloch sphere. Pure states represent the two states at the band crossing point before inducing SOC. Two mixing states represent the electron and hole after the inclusion of interlevel SOC interaction. Four panels around the Bloch sphere are the schematic diagram of the inverted bands before and after the inclusion of SOC, in which solid lines correspond to the points on the Bloch sphere. Horizontal dashed gray lines represent Fermi levels.

momenta, \mathbf{S} and \mathbf{L} , vary in this process, we scrutinize the SOC interaction at the band crossing point. We treat the two eigenstates at the band crossing point before inducing SOC as a two-level system, described by the Hamiltonian:

$$H_0 = \begin{pmatrix} E_1 & \\ & E_2 \end{pmatrix}, \quad (1)$$

where $E_{1/2}$ denote energies of the two unperturbed states. Then we added the perturbation (interlevel SOC interaction $\hat{H}_{\text{soc}} = \lambda \hat{\mathbf{L}} \cdot \hat{\mathbf{S}}$, where λ represents the interaction strength) to this system which induces an interlevel coupling:

$$H = \begin{pmatrix} E_1 & H_{\text{soc}} \\ H_{\text{soc}}^* & E_2 \end{pmatrix} \quad (2)$$

(see Sec. I in the Supplemental Material [32]). Through the orthogonality of eigenstates, we know that the interlevel perturbation from SOC gives rise to a total angular-momentum difference δj_z between the new eigenstates, namely, the ultimate electron and hole around the Fermi level. Specifically, the requirement for the unperturbed states to interact with each other sets a limit to their angular momenta, which indicates a zero angular-momentum difference before SOC interaction ($\delta s_z + \delta l_z = 0$) [33]. Hence, the resultant inter-level δj_z serves as a unique characteristic of the inter-level SOC interaction. This can be sketched on a Bloch sphere [Fig. 1(a)]. The north and south poles represent two unperturbed states without coupling and Berry phase. The SOC interaction induces the mixing of two unperturbed states and sets opposite Berry

phases to the electron and hole. As a result, the production of the local Berry curvature is accompanied by the emergence of δj_z , which are two simultaneous processes.

To quantitatively reveal the correspondence between such an angular-momentum difference and the quantized Hall conductance, we examine systems that exhibit discrete rotation symmetries C_n , where n equals 2, 3, 4, or 6, along the z axis, with the inclusion of out-of-plane magnetization. In this context, all unitary components of the resultant magnetic space group are reduced to the cyclic group (Sec. II, Table S2 in the Supplemental Material [32]). Given that angular momentum is the generator of the rotation operator, potential values of j_z for the electronic state on the rotation axis can be derived. The eigenspinors with the eigenvalue of the rotation operator $\exp(\pm i j_z \frac{2\pi}{n})$ are bisected on the complex plane, as depicted in Figs. 2(a)–2(d) (Sec. II, Table S3 in the Supplemental Material [32]).

We subsequently examine possible values of the angular-momentum differences, denoted as $\delta j_z = j_c - j_v$, where j_c and j_v represent the total angular momentum of conduction and valence bands at the band crossing point after inducing SOC. It is noteworthy that δj_z is quantized with a minimum unit of ± 1 , correlating to the phase difference $\exp(\pm i \frac{2\pi}{n})$ under rotation operation, as demonstrated by the curved red arrows in Figs. 2(a)–2(d). Moreover, under rotation constraint, $j'_z = j_z + pn$ ($p = 0, \pm 1, \pm 2, \dots$) equates to j_z . For instance, $j'_z = -\frac{3}{2}$ and $j_z = \frac{3}{2}$ at a C_3 rotation axis are equivalent [Fig. 2(b)]. Consequently, the angular-momentum differences $\delta j_z = -\frac{3}{2} - \frac{1}{2} = -2$ and $\delta j_z = \frac{3}{2} - \frac{1}{2} = 1$ at a C_3 rotation invariant point both signify the phase difference $\exp(i \frac{2\pi}{3})$ [Fig. 2(b)]. In this context, we use a quantized $l_{\delta z} = \delta j_z + pn$ to denote all δj_z 's with the actual phase difference $\exp(i l_{\delta z} \frac{2\pi}{n})$ under the effect of rotation operation C_n , $n = 2, 3, 4$, and 6, where $l_{\delta z}$ is within the range $[-n/2, n/2]$.

Thus, inspired by the quantization of $l_{\delta z}$ under rotation symmetries, it is natural to ask how the two nonzero quantized properties link exactly in the QAHE: the Hall conductance and the interlevel angular-momentum difference. To unveil this plausible connection, we built a $\mathbf{k} \cdot \mathbf{p}$ model by considering the leading term (symmetry-allowed lowest order) (Sec. III A in the Supplemental Material [32]):

$$h(\mathbf{k}) = \begin{bmatrix} \frac{\Delta}{2} & \exp(-i l_{\delta z} \phi) \\ \exp(i l_{\delta z} \phi) & -\frac{\Delta}{2} \end{bmatrix}, \quad (3)$$

where $\phi = \arctan(\frac{k_x}{k_y})$ is the azimuthal angle in momentum space circling the crossing point, and Δ is the band gap with positive values.

The contributed Hall conductance from the effective model is equal to the Berry phase integration around the center of the model [34] (Sec. III B in the Supplemental Material [32]):

$$\sigma_{xy}^H = \frac{l_{\delta z}}{2} \frac{e^2}{\hbar}. \quad (4)$$

It is evident that the Hall conductance exhibits a direct proportionality to the effective angular momentum, denoted as $l_{\delta z}$, as defined herein. Specifically, when $l_{\delta z} = +1$ ($l_{\delta z} = -1$), the Hall conductance σ_{xy}^H is equal to the half-quantized value $\frac{e^2}{2\hbar}$ ($-\frac{e^2}{2\hbar}$), as indicated in Fig. 2(e), the scenario where

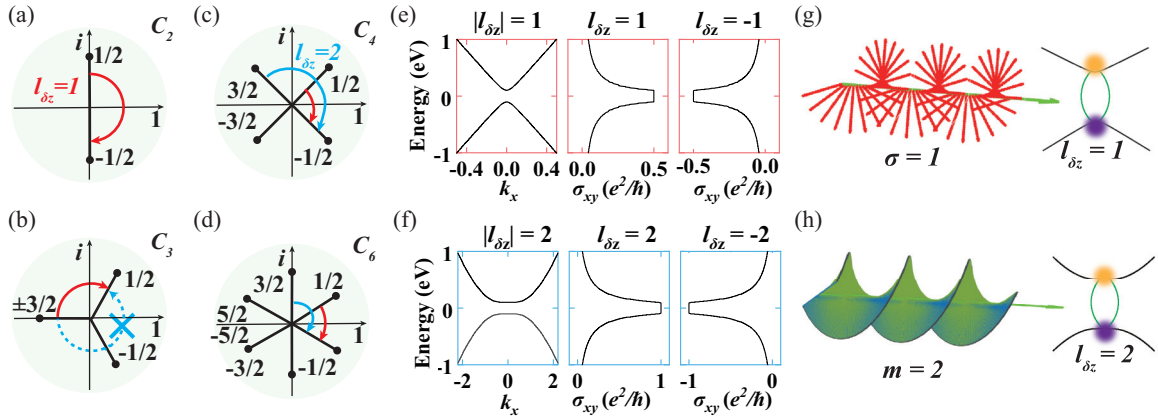


FIG. 2. Classification of the conductance δj_z correspondence via rotation symmetries. (a)–(d) Possible values of j_z and the eigenvalue of the generated rotation operator $\exp(\pm i j_z \frac{2\pi}{n})$ on the complex plane, where $n = 2, 3, 4$, and 6 correspond to rotation symmetries C_2 , C_3 , C_4 , and C_6 , respectively. The cambered red (cyan) arrows represent $l_{\delta z} = 1$ (2). (e) The band structure and Hall conductance calculated from Eq. (3) when $|l_{\delta z}| = 1$, in which the dispersion is linear, and $l_{\delta z} = +1$ ($l_{\delta z} = -1$) gives rise to positive (negative) half-quantized Hall conductance. (f) Same as (e) but for $|l_{\delta z}| = 2$, in which the dispersion is quadratic, and $l_{\delta z} = +2$ ($l_{\delta z} = -2$) gives rise to positive (negative) quantized Hall conductance. (g) The sketch of light absorption of right-handed circularly polarized light in a quantum anomalous Hall insulator (QAH) with interlevel angular-momentum difference $l_{\delta z} = 1$. The light carries spin angular momentum $\sigma = 1$ but zero orbital angular momentum $m = 0$. The total angular momentum of the electron (orange ball) and the photon before excitation should be equal to the electron (purple ball) after excitation. (h) The sketch of light absorption of photons carrying orbital angular momentum $m = 2$ (with zero spin angular momentum $\sigma = 0$) in a QAH with $l_{\delta z} = 2$.

$l_{\delta z} = \pm 1$ corresponds to the gapping of a linear Dirac cone [34]. According to the no-go theorem, gapped linear Dirac cones are expected to manifest in pairs throughout the Brillouin zone [35,36]. Thus, two gapped linear Dirac cones possessing $|l_{\delta z}| = 1$ are needed to yield quantized Hall conductance.

Under C_4 or C_6 rotations, the effective angular momentum $|l_{\delta z}|$ can also equal 2, as indicated by cyan arrows Figs. 2(c) and 2(d). Consequently, when $l_{\delta z} = \pm 2$, the contributed Hall conductance is equal to $\pm \frac{e^2}{h}$. This can be understood as massive double-Dirac fermions with quadratic dispersions [Fig. 2(f)].

In an insulator without time-reversal symmetry, multiple band crossing may occur either at a single point or at multiple points across the entire momentum space. In such cases, the total Hall conductance for the system can be expressed as $\sigma_{xy}^H = \sum_1^a l_{\delta z, a} \frac{e^2}{2h}$, where a represents the count of the band crossing points featuring angular-momentum difference $l_{\delta z, a}$. To exemplify this, we built a magnetic triangle lattice model with three band crossing points, two at K points with C_3 rotation and one at Γ with C_6 rotation (Sec. IV in the Supplemental Material [32]). In accordance with our theoretical framework, we observed that, at K points, $l_{\delta z} = -1$ and $\sigma_{xy}^H = -\frac{1}{2} \frac{e^2}{h}$, while at Γ , $l_{\delta z} = 2$ and $\sigma_{xy}^H = \frac{e^2}{h}$ were obtained.

We further discuss the light absorption of a QAH in the case of quantized $l_{\delta z}$ due to the preservation of rotation symmetries. The light transition from the SOC-forced electron to the hole is scrutinized, where the photon possesses angular momentum, denoted j^L . In line with the principle of angular-momentum conservation, the angular momenta of the electron and photon remain constant, as defined by the equation $j_c = j_v + j^L$ [37]. This observation elucidates that the discerned value of $l_{\delta z}$ within a QAH corresponds to the momentum

of the absorbed photon, that is, $l_{\delta z} = j^L$, thereby highlighting the presence of selective light absorption. For instance, when $l_{\delta z} = 1$, the QAH tends to absorb right-circularly polarized light, characterized by a spin polarization of $\sigma = 1$, as opposed to left-circularly polarized light ($\sigma = -1$) [Fig. 2(g)]. This phenomenon is recognized as the quantized magnetic circular dichroism effect. Moreover, a QAH with an absolute value of $l_{\delta z} \geq 2$ is a potential candidate for realizing the magnetic circular dichroism effect for lasers with quantized orbital angular momentum > 1 [Fig. 2(h)]. Now we directly verify our findings with real materials, specifically MnBi_2Te_4 [24,38–45] and Cr-doped Sb_2Te_3 [6,7,46,47]. The two materials have been previously experimentally identified as QAHs with opposite Chern numbers [6,24]. Thanks to their retention of C_3 rotation symmetry, it becomes feasible to evaluate the angular momentum using first-principles calculations directly [48]. Figure 3(a) represents the band structure of three septuple layers (SLs) of MnBi_2Te_4 near the Γ point. A Chern number -1 arises from the TI Dirac cones at the top and bottom surfaces [Figs. 3(a) and S3 in the Supplemental Material]. The energy-increasing ordered angular momenta of the four bands in MnBi_2Te_4 are $+\frac{1}{2}$, $+\frac{1}{2}$, $-\frac{1}{2}$, $-\frac{1}{2}$. The momentum-resolved circularly polarized light absorption calculations show that left-handed light, with $\sigma = -1$, is absorbed [Fig. 3(b)]. Conforming to our theory, the local dispersions proximate to these four states in MnBi_2Te_4 could be conceptualized as two linear gapped Dirac cones with $l_{\delta z} = -1 - 1 = -2$ [Fig. 2(e)]. In stark contrast, although similar bands with gapped linear Dirac cones are observed in Cr-doped Sb_2Te_3 , the sign of the Berry curvature in this material is inverted [Fig. 3(c)]. Our calculations further demonstrate that the effective angular momentum $l_{\delta z}$ is also inverted from -2 to 2 in Cr-doped Sb_2Te_3 , as evidenced by the absorption of right-handed light associated with a positive $l_{\delta z}$ [Fig. 3(d)].

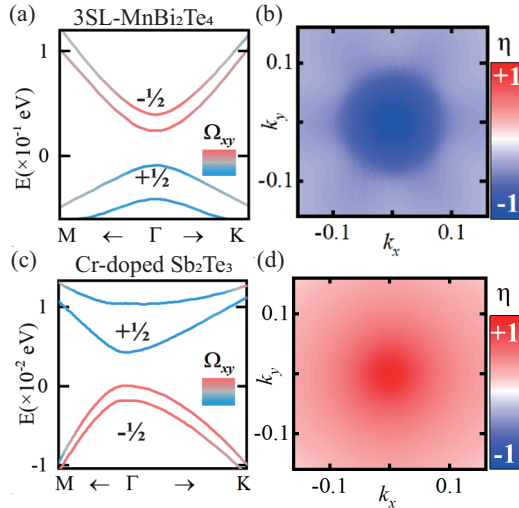


FIG. 3. Local Berry curvature and circularly polarized light-transition in real materials. (a) Berry curvature-colored bands of 3-SL MnBi_2Te_4 around the Γ point, where the bands cross. The pseudototal angular momenta j_z are labeled. (b) Simulation of the intensity of interband light transition η of 3-SL MnBi_2Te_4 . $\eta(\mathbf{k}) = \frac{|P_+(\mathbf{k})|^2 - |P_-(\mathbf{k})|^2}{|P_+(\mathbf{k})|^2 + |P_-(\mathbf{k})|^2}$, where P_+ (P_-) is the transition matrix element of right-handed (left-handed) circularly polarized light [49]. (c) and (d) Same as (a) and (b) but for Cr-doped Sb_2Te_3 around the Γ point.

To understand the chiral orbiting in the QAHE, we further discuss the anomalous transport of an electron in the intrinsic QAHE by contrast with metal conducting. In band theory, metal conducting is regarded as that the electronic state around the Fermi level will drift toward the adjacent-momentum state since the spatial amplitude distribution of the wave function is continuously varied in the momentum space, and two adjacent-momentum states have similar spatial amplitude distributions [Fig. 4(a)]. In the scenario of band crossing and SOC-forced gapping, and for one of the bands, SOC only impacts the angular momenta, so the spatial amplitude distribution of the wave function is still delocalized [50] and continuously varying in terms of momentum. Hence, the electron near the Fermi level which tends to drift along the electrical field is obstructed by the energy gap and expected to adjust its angular momentum by $l_{\delta z}$ to reach the adjacent-momentum state (the hole state) [Fig. 4(b)]. Since $l_{\delta z}$ is totally from the interlevel coupling between spin and orbital angular momenta [Fig. 1(a)], the electron should not only spin intrinsically but also orbit in the real space [51] to achieve the ladder or lower of the total angular momentum.

Then the connection between the magnetization \mathbf{M} and the magnetic-field-like $l_{\delta z}$ in a QAHI can also be illustrated. In the classical QHE, electron motion within a magnetic field is driven by the Lorentz force $\mathbf{F} = -e\mathbf{v} \times \mathbf{B}$, wherein the external magnetic field and the skipping orbits on the edge conform to the left-hand rule [2,3]. Thus, flipping the direction of the magnetic field can invert the direction of skipping orbits. In contrast, within a field-free QAHI, although inverting the direction of magnetization \mathbf{M} can flip the Hall current, no established chirality exists between the Hall current and a true effective field. Instead, there are two opposite loops of magnetic field dependence of σ_{xy}^H in MnBi_2Te_4 [Fig. 4(c)]

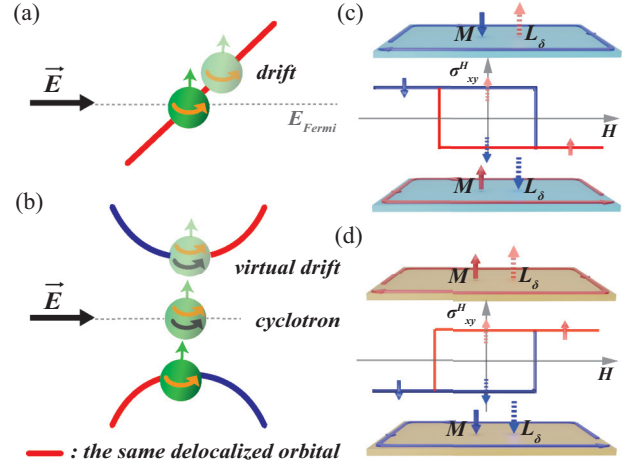


FIG. 4. $l_{\delta z}$ -forced orbiting of an electron and the chirality of a quantum anomalous Hall insulator (QAHI). (a) In metal, the delocalized orbital lies on the Fermi level, in which the electron (green balls with arrows which represent spin axes) could drift freely in terms of the electrical field. In this case, there is no change of angular momentum (yellow curved arrow). (b) In a QAHI, one delocalized orbital is split and distributed around the Fermi level. The electron state under the electrical field which tends to drift toward the hole state in one delocalized orbital should experience a ladder (or lower) of the total angular momentum (black curved arrow) and subsequently orbit in the real space. (c) The Hall current is locked with \mathbf{L}_{δ} by the left-hand rule. When \mathbf{L}_{δ} (dash arrow) and \mathbf{M} (solid arrow) are antiparallel to each other, the field-dependence Hall conductance loop is shown by the middle panel. We use a cyan-colored slab to represent the QAHI in which \mathbf{L}_{δ} and \mathbf{M} are antiparallel to each other. (d) Same as (c), the Hall current is still locked with \mathbf{L}_{δ} by the left-hand rule. The brown-colored slab represents the QAHI in which \mathbf{L}_{δ} and \mathbf{M} are parallel to each other.

and Cr-doped Sb_2Te_3 [Fig. 4(d)]. With the understanding of the chiral orbiting from $l_{\delta z}$, we now represent $l_{\delta z}$ through an effective field \mathbf{L}_{δ} , where a positive (negative) z direction represents $l_{\delta z} > 0$ ($l_{\delta z} < 0$), as indicated by the dashed arrows in Figs. 4(c) and 4(d). Interestingly, both MnBi_2Te_4 and Cr-doped Sb_2Te_3 exhibit left handedness between the effective field \mathbf{L}_{δ} and the Hall current. Hence, by mapping the internal orbital field \mathbf{L}_{δ} to the external magnetic field \mathbf{H} and the anomalous Hall current onto the skipping orbit on the edge, an analog of the classical QHE [52] in a QAHI is built.

The two opposite loops of the magnetic-field-dependent Hall current [6,24] in a QAHI can be explained by the relative orientation between \mathbf{M} and \mathbf{L}_{δ} . More specifically, when \mathbf{M} is antiparallel (parallel) to \mathbf{L}_{δ} , the Hall current concerning \mathbf{M} adheres to a right-hand (left-hand) rule [Figs. 4(c) and 4(d)]. In a ferromagnetic QAHI, a \mathbf{M} reversal by the magnetic field is equivalent to a spin \mathbf{S} inversion. Because of the fixed sign of $\mathbf{L} \cdot \mathbf{S}$, the orbital \mathbf{L} aligns with the spin \mathbf{S} . As a result, total angular momentum \mathbf{J} and effective angular momentum $l_{\delta z}$ and \mathbf{L}_{δ} will also flip subject to inversion of \mathbf{M} , inducing the sign change of the Hall conductance. The relative orientation of \mathbf{M} and \mathbf{L}_{δ} is fixed within a material, leading to the preservation of the magnetic-field-dependent loop with a fixed chirality. To realize the transition of the magnetic-field-dependent Hall current loop from one handedness to the other, modifications to

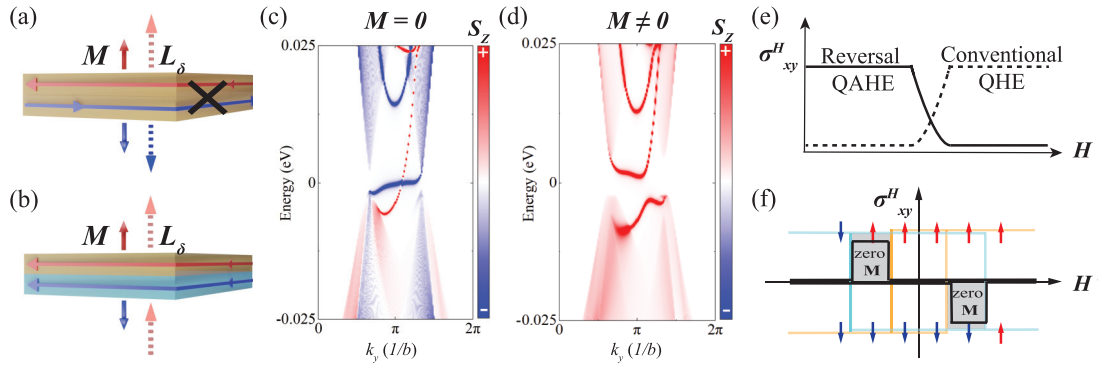


FIG. 5. Spin-momentum-unlocking edge states and reversal quantum anomalous Hall effect (QAHE) in an antiferromagnetic (AFM) quantum anomalous Hall insulator (QAHI). (a) and (b) Double-layer system with the same (opposite) chirality QAHE systems. Magnetization direction \mathbf{M} and sign of angular-momentum difference \mathbf{L}_δ are labeled by solid and dashed arrows, in which red (blue) represents upward (downward) direction and positive (negative) sign. Spin-up (down) states of the edge are labeled by the horizontal red (blue) arrow. (c) and (d) Spin-resolved edge states for a double-layer system in (b) stacked by monolayer PdBr_3 and PdCl_3 with zero and nonzero net total magnetization but nonzero and zero total $l_{\delta z}$. (e) Schematic of reversal QAHE in comparison with conventional QAHE. (f) Schematic of field-dependence QAHE loop, in which the reversal QAHE can be realized at the region of hysteresis difference (black line) of two opposite QAHE systems (orange and cyan lines).

the internal properties of the system are required. One feasible method entails altering the signs of SOC. To exemplify this, we use PdBr_3 and PdCl_3 , which are predicted to be QAHIs with Chern numbers of opposite signs. Our first-principles calculations show they exhibit opposite signs of $l_{\delta z}$ due to the opposite signs of SOC (Figs. S4 and S5 in the Supplemental Material [32]).

In a ferromagnetic QAHI, we have shown that magnetization \mathbf{M} is indirectly linked to the Hall conductance σ_{xy}^H through interlevel angular-momentum difference. We then utilize the reality of decoupling \mathbf{M} and σ_{xy}^H and design a QAHI with zero total magnetic moment. The entire internal effective orbital field of the system can be expressed as $\mathbf{L}_\delta^{\text{total}} = \mathbf{L}_\delta^{\text{top}} + \mathbf{L}_\delta^{\text{bottom}}$. In a conventional case, both layers possess the same relative orientation between \mathbf{L}_δ and \mathbf{M} , and $\mathbf{L}_\delta^{\text{total}}$ of the whole system cancels out if the magnetizations in the two layers are oppositely oriented [Fig. 5(a)]. As a result, quantized edge states are gapped out [24,45,53]. However, if \mathbf{L}_δ and \mathbf{M} are in opposite relative orientations in two layers, the total $\mathbf{L}_\delta^{\text{total}}$ is nonzero even when the total magnetization (\mathbf{M}) cancels out [Fig. 5(b)]. In this case, two copropagating chiral modes of opposite spin directions can be protected with net zero magnetization [Fig. 5(c)], whereas the edges will be gapped when the system is in ferromagnetic orders [Fig. 5(d)]. This means that, in a QAHI with a net zero magnetization, $|\sigma_{xy}^H|$ will drop to zero as the external magnetic field increases to a critical point [Fig. 5(e)]. To emphasize the unconventional magnetic responses of the QAHE with net zero magnetization, we introduce the term *reversal QAHE* as a distinctive label from its conventional counterpart.

Though a QAHI has been recognized as an ideal resistance standard in quantum metrology [54], the stray magnetic fields from a traditional QAHI could interfere with other sensitive quantum devices, thereby limiting their integration and broader use. In contrast, the reversal QAHE could lead to the development of highly efficient, low-power-consumption devices with minimized interference. The manifestation of the

reversal QAHE within the Bi_2Te_3 family is indeed feasible in experiments. One proposed methodology involves the layered stacking of MnBi_2Te_4 and Cr-doped Sb_2Te_3 [9]. Notably, even if the Cr and Mn atoms exhibit identical magnetization directions within the sample, their coercive field strengths can be exploited to establish opposite magnetization directions between them [Fig. 5(f)] [55]. An alternative method involves magnetizing the top (bottom) surface of the Bi_2Te_3 thin film by doping Mn (Cr) atoms independently. This becomes feasible under weak magnetic fields when the top and bottom surfaces are adequately separated from each other. It is worth noting that both methodologies necessitate precise control of the doping level of Cr atoms. The objective is to ensure that the net magnetization induced by the Cr atoms is equivalent to that from the Mn atoms.

In summary, we show that the QAHE can be associated with an angular-momentum difference between the electron and hole around Fermi level, which also gives rise to a unique magnetic circular dichroism effect. With the introduction of an effective internal field stemming from the angular momentum, we illustrate the force of chiral orbiting in the QAHE. It further paves the way for understanding an axion insulator [45] and the layer Hall effect [56] with alternative spin configurations.

We acknowledge Chao-xing Liu, Justin CW Song, and Baile Zhang for their useful conversations. We thank Zhiming Xu for offering the information of crystal structures of QAHIs. This paper is supported by the National Research Foundation (NRF), Singapore, under its Fellowship Award (Grant No. NRF-NRFF13-2021-0010) and the Nanyang Assistant Professorship grant (Grant No. NTUSUG). B.Y. is supported by the NRF, Singapore, under the NRF fellowship award (Grant No. NRF-NRFF12-2020-005). S.-Y.X. and Q.M. acknowledge the support from the Center for the Advancement of Topological Semimetals, an Energy Frontier Research Center funded by the U.S. Department of Energy

Office of Science, through the Ames Laboratory under Contract No. DEAC02-07CH11358. J.-X.Y. acknowledges the support from the National Key R&D Program of China (Grant No. 2023YFA1407300) and the National Science Foundation of China (Grant No. 12374060). W.-B.G. acknowledges

the financial support from the National Research Foundation (NRF), Singapore through its Competitive Research Program (CRP Award No. NRF-CRP22-2019-0004).

H.C., Y.J., and M.Y. contributed equally to this work.

-
- [1] K. v. Klitzing, G. Dorda, and M. Pepper, *Phys. Rev. Lett.* **45**, 494 (1980).
- [2] R. B. Laughlin, *Phys. Rev. B* **23**, 5632(R) (1981).
- [3] B. I. Halperin, *Phys. Rev. B* **25**, 2185 (1982).
- [4] F. D. M. Haldane, *Phys. Rev. Lett.* **61**, 2015 (1988).
- [5] R. Yu, W. Zhang, H.-J. Zhang, S.-C. Zhang, X. Dai, and Z. Fang, *Science* **329**, 61 (2010).
- [6] C.-Z. Chang, J. Zhang, X. Feng, J. Shen, Z. Zhang, M. Guo, K. Li, Y. Ou, P. Wei, L.-L. Wang *et al.*, *Science* **340**, 167 (2013).
- [7] J. G. Checkelsky, R. Yoshimi, A. Tsukazaki, K. S. Takahashi, Y. Kozuka, J. Falson, M. Kawasaki, and Y. Tokura, *Nat. Phys.* **10**, 731 (2014).
- [8] C.-X. Liu, S.-C. Zhang, and X.-L. Qi, *Annu. Rev. Condens. Matter Phys.* **7**, 301 (2016).
- [9] Y. Tokura, K. Yasuda, and A. Tsukazaki, *Nat. Rev. Phys.* **1**, 126 (2019).
- [10] C.-Z. Chang, C.-X. Liu, and A. H. MacDonald, *Rev. Mod. Phys.* **95**, 011002 (2023).
- [11] M. Z. Hasan and C. L. Kane, *Rev. Mod. Phys.* **82**, 3045 (2010).
- [12] N. Nagaosa, J. Sinova, S. Onoda, A. H. MacDonald, and N. P. Ong, *Rev. Mod. Phys.* **82**, 1539 (2010).
- [13] X.-L. Qi and S.-C. Zhang, *Rev. Mod. Phys.* **83**, 1057 (2011).
- [14] A. Bansil, H. Lin, and T. Das, *Rev. Mod. Phys.* **88**, 021004 (2016).
- [15] X.-G. Wen, *Rev. Mod. Phys.* **89**, 041004 (2017).
- [16] N. P. Armitage, E. J. Mele, and A. Vishwanath, *Rev. Mod. Phys.* **90**, 015001 (2018).
- [17] M. Z. Hasan, G. Chang, I. Belopolski, G. Bian, S.-Y. Xu, and J.-X. Yin, *Nat. Rev. Mater.* **6**, 784 (2021).
- [18] B. Q. Lv, T. Qian, and H. Ding, *Rev. Mod. Phys.* **93**, 025002 (2021).
- [19] L. Fu, C. L. Kane, and E. J. Mele, *Phys. Rev. Lett.* **98**, 106803 (2007).
- [20] Y. Xia, D. Qian, D. Hsieh, L. Wray, A. Pal, H. Lin, A. Bansil, D. Grauer, Y. S. Hor, R. J. Cava *et al.*, *Nat. Phys.* **5**, 398 (2009).
- [21] X.-L. Qi, T. L. Hughes, and S.-C. Zhang, *Phys. Rev. B* **78**, 195424 (2008).
- [22] C. Fang, M. J. Gilbert, X. Dai, and B. A. Bernevig, *Phys. Rev. Lett.* **108**, 266802 (2012).
- [23] A. L. Sharpe, E. J. Fox, A. W. Barnard, J. Finney, K. Watanabe, T. Taniguchi, M. A. Kastner, and D. Goldhaber-Gordon, *Science* **365**, 605 (2019).
- [24] Y. Deng, Y. Yu, M. Z. Shi, Z. Guo, Z. Xu, J. Wang, X. H. Chen, and Y. Zhang, *Science* **367**, 895 (2020).
- [25] Y. Xu, L. Elcoro, Z.-D. Song, B. J. Wieder, M. G. Vergniory, N. Regnault, Y. Chen, C. Felser, and B. A. Bernevig, *Nature (London)* **586**, 702 (2020).
- [26] H. Deng, Z. Chen, A. Wołos, M. Konczykowski, K. Sobczak, J. Sitnicka, I. V. Fedorchenko, J. Borysiuk, T. Heider, Ł. Pluciński *et al.*, *Nat. Phys.* **17**, 36 (2021).
- [27] S. Nakatsuji, N. Kiyohara, and T. Higo, *Nature (London)* **527**, 212 (2015).
- [28] Z. Xu, W. Duan, and Y. Xu, *Nano Lett.* **23**, 305 (2023).
- [29] Y. Liu, J. Li, and Q. Liu, *Nano Lett.* **23**, 8650 (2023).
- [30] M. S. Alam, A. Fakhredine, M. Ahmad, P. K. Tanwar, H.-Y. Yang, F. Tafti, G. Cuono, R. Islam, B. Singh, A. Lynnyk *et al.*, *Phys. Rev. B* **107**, 085102 (2023).
- [31] T. C. van Thiel, W. Brzezicki, C. Autieri, J. R. Hortensius, D. Afanasiev, N. Gauquelin, D. Jannis, N. Janssen, D. J. Groenendijk, J. Fatemans *et al.*, *Phys. Rev. Lett.* **127**, 127202 (2021).
- [32] See Supplemental Material at <http://link.aps.org/supplemental/10.1103/PhysRevB.109.125305> for supplemental notes, Figs. S1–S5, and Tables S1–S3, which includes Refs. [22,33,34,57–69].
- [33] Z. Liu, G. Zhao, B. Liu, Z. F. Wang, J. Yang, and F. Liu, *Phys. Rev. Lett.* **121**, 246401 (2018).
- [34] K. Everschor-Sitte, M. Sitte, and A. H. MacDonald, *Phys. Rev. B* **92**, 245118 (2015).
- [35] H. B. Nielsen and M. Ninomiya, *Nucl. Phys. B* **185**, 20 (1981).
- [36] H. B. Nielsen and M. Ninomiya, *Nucl. Phys. B* **193**, 173 (1981).
- [37] W. Yao, D. Xiao, and Q. Niu, *Phys. Rev. B* **77**, 235406 (2008).
- [38] S.-Y. Xu, M. Neupane, C. Liu, D. Zhang, A. Richardella, L. A. Wray, N. Alidoust, M. Leandersson, T. Balasubramanian, and J. Sánchez-Barriga *et al.*, *Nat. Phys.* **8**, 616 (2012).
- [39] J. Li, Y. Li, S. Du, Z. Wang, B.-L. Gu, S.-C. Zhang, K. He, W. Duan, and Y. Xu, *Sci. Adv.* **5**, eaaw5685 (2019).
- [40] M. M. Otrokov, I. P. Rusinov, M. Blanco-Rey, M. Hoffmann, A. Yu. Vyazovskaya, S. V. Eremeev, A. Ernst, P. M. Echenique, A. Arnau *et al.*, *Phys. Rev. Lett.* **122**, 107202 (2019).
- [41] M. M. Otrokov, I. I. Klimovskikh, H. Bentmann, D. Estyunin, A. Zeugner, Z. S. Aliev, S. Gaß, A. U. B. Wolter, A. V. Koroleva, A. M. Shikin *et al.*, *Nature (London)* **576**, 416 (2019).
- [42] Y.-J. Hao, P. Liu, Y. Feng, X.-M. Ma, E. F. Schwier, M. Arita, S. Kumar, C. Hu, R. Lu, M. Zeng *et al.*, *Phys. Rev. X* **9**, 041038 (2019).
- [43] Y. J. Chen, L. X. Xu, J. H. Li, Y. W. Li, H. Y. Wang, C. F. Zhang, H. Li, Y. Wu, A. J. Liang, C. Chen *et al.*, *Phys. Rev. X* **9**, 041040 (2019).
- [44] H. Li, S.-Y. Gao, S.-F. Duan, Y.-F. Xu, K.-J. Zhu, S.-J. Tian, J.-C. Gao, W.-H. Fan, Z.-C. Rao, J.-R. Huang *et al.*, *Phys. Rev. X* **9**, 041039 (2019).
- [45] C. Liu, Y. Wang, H. Li, Y. Wu, Y. Li, J. Li, K. He, Y. Xu, J. Zhang, and Y. Wang, *Nat. Mater.* **19**, 522 (2020).
- [46] L. A. Wray, S.-Y. Xu, Y. Xia, D. Hsieh, A. V. Fedorov, Y. S. Hor, R. J. Cava, A. Bansil, H. Lin, and M. Z. Hasan, *Nat. Phys.* **7**, 32 (2011).
- [47] A. J. Bestwick, E. J. Fox, X. Kou, L. Pan, K. L. Wang, and D. Goldhaber-Gordon, *Phys. Rev. Lett.* **114**, 187201 (2015).
- [48] J. Gao, Q. Wu, C. Persson, and Z. Wang, *Comput. Phys. Commun.* **261**, 107760 (2021).
- [49] G. Chang, J.-X. Yin, T. Neupert, D. S. Sanchez, I. Belopolski, S. S. Zhang, T. A. Cochran, Z. J. Chéng, M.-C. Hsu, S.-M. Huang *et al.*, *Phys. Rev. Lett.* **124**, 166404 (2020).

- [50] B. Bradlyn, L. Elcoro, J. Cano, M. G. Vergniory, Z. Wang, C. Felser, M. I. Aroyo, and B. A. Bernevig, *Nature (London)* **547**, 298 (2017).
- [51] L. H. I. Thomas, *London, Edinburgh Dublin Philos. Mag. J. Sci.* **3**, 1 (1927).
- [52] J. M. Luttinger, *Phys. Rev.* **102**, 1030 (1956).
- [53] Y.-F. Zhao, R. Zhang, R. Mei, L.-J. Zhou, H. Yi, Y.-Q. Zhang, J. Yu, R. Xiao, K. Wang, N. Samarth *et al.*, *Nature (London)* **588**, 419 (2020).
- [54] Y. Okazaki, T. Oe, M. Kawamura, R. Yoshimi, S. Nakamura, S. Takada, M. Mogi, K. S. Takahashi, A. Tsukazaki, M. Kawasaki *et al.*, *Nat. Phys.* **18**, 25 (2022).
- [55] M. Mogi, M. Kawamura, A. Tsukazaki, R. Yoshimi, K. S. Takahashi, M. Kawasaki, and Y. Tokura, *Sci. Adv.* **3**, ea01669 (2017).
- [56] A. Gao, Y.-F. Liu, C. Hu, J.-X. Qiu, C. Tzschaschel, B. Ghosh, S.-C. Ho, D. Bérubé, R. Chen, H. Sun *et al.*, *Nature (London)* **595**, 521 (2021).
- [57] G. F. Koster, J. O. Dimmock, R. G. Wheeler, and H. Statz, *Properties of the Thirty-Two Point Groups* (The MIT Press, Cambridge, 1963).
- [58] C. J. Bradley and A. P. Cracknell, *The Mathematical Theory of Symmetry in Solids: Representation Theory for Point Groups and Space Groups* (Clarendon Press, Oxford, 1972).
- [59] J. Zhang, B. Zhao, Y. Xue, T. Zhou, and Z. Yang, *Phys. Rev. B* **97**, 125430 (2018).
- [60] Y.-P. Wang, S.-S. Li, C.-W. Zhang, S.-F. Zhang, W.-X. Ji, P. Li, and P.-J. Wang, *J. Mater. Chem. C* **6**, 10284 (2018).
- [61] J.-Y. You, Z. Zhang, B. Gu, and G. Su, *Phys. Rev. Appl.* **12**, 024063 (2019).
- [62] G. Kresse and J. Furthmüller, *Phys. Rev. B* **54**, 11169 (1996).
- [63] J. P. Perdew, K. Burke, and M. Ernzerhof, *Phys. Rev. Lett.* **77**, 3865 (1996).
- [64] P. E. Blöchl, *Phys. Rev. B* **50**, 17953 (1994).
- [65] S. Grimme, J. Antony, S. Ehrlich, and H. Krieg, *J. Chem. Phys.* **132**, 154104 (2010).
- [66] A. Tkatchenko and M. Scheffler, *Phys. Rev. Lett.* **102**, 073005 (2009).
- [67] M. P. L. Sancho, J. M. L. Sancho, J. M. L. Sancho, and J. Rubio, *J. Phys. F: Met. Phys.* **15**, 851 (1985).
- [68] N. Marzari and D. Vanderbilt, *Phys. Rev. B* **56**, 12847 (1997).
- [69] I. Souza, N. Marzari, and D. Vanderbilt, *Phys. Rev. B* **65**, 035109 (2001).